

Artifacts in optical projection tomography due to refractive index mismatch: model and correction

YAN LIU¹, JONATHAN DONG¹, CÉDRIC SCHMIDT², ALEIX BOQUET-PUJADAS¹, JÉRÔME EXTERMANN², AND MICHAEL UNSER^{1,*}

¹Biomedical Imaging Group, École Polytechnique Fédérale Lausanne, Station 17, 1015 Lausanne, Switzerland

²HEPIA/HES-SO, University of Applied Sciences of Western Switzerland, Rue de la Prairie 4, 1202 Geneva, Switzerland

*Corresponding author: michael.unser@epfl.ch

Compiled April 2, 2022

Optical Projection Tomography (OPT) is a powerful tool for 3D imaging of mesoscopic samples, thus of great importance to image whole organs for the study of various disease models in life sciences. OPT is able to achieve resolution at a few tens of microns over a large sample volume of several cubic centimeters. However, the reconstructed OPT images often suffer from artifacts caused by different kinds of physical miscalibration. This work focuses on the refractive index (RI) mismatch between the rotating object and the surrounding medium. We derive a 3D cone beam forward model to approximate the effect of RI mismatch and implement a fast and efficient reconstruction method to correct the induced seagull-shaped artifacts on experimental images of fluorescent beads.

© 2022 Optical Society of America

<http://dx.doi.org/10.1364/ao.XX.XXXXXX>

Since its invention by J. Sharpe in 2002 [1, 2], Optical Projection Tomography (OPT) has become a powerful tool to obtain three-dimensional images of biological tissues at the mesoscopic scale [3–5]. Thanks to its increased penetration depth [6], it can image whole animals at a resolution of a few tens of microns [4] with molecular specificity [3, 4]. Often referred to as the optical analog of X-ray CT [7], OPT works with non-ionizing light, thereby minimizing radiation damage and facilitating longitudinal studies of a broad range of diseases including Alzheimer's [8] and gastrointestinal pathologies [4].

However, one frequently observes various artifacts in OPT images, which can stem from a range of different reasons. They may come from mechanical errors in the imaging system: for instance, a misaligned rotation center will generate double-edge or circle artifacts in the reconstruction [9–11]. Unstabilities such as illumination fluctuation and detector sensitivity variation will cause smear and ring artifacts [9]. Finally, deviations from the ideal physical model may arise such as the finite depth-of-field of the imaging system [2] or a refraction that perturbs light propa-

gation [6, 12]. All these artifacts come from a mismatch between the idealized OPT model and the actual physical realization. They strongly degrade the final resolution and quality of the reconstructed OPT images, but can be corrected computationally once they have been properly identified [9, 10].

Recently, when using fluorescent beads to assess the resolution of an emission OPT imaging system, OPT practitioners observed seagull-shaped artifacts suspected to be a result of refractive index (RI) mismatch between the sample and its embedding medium [4]. During an OPT experiment, the sample is typically fixed in a cylindrical gel phantom that is immersed in an index-matching liquid [2, 13, 14] to avoid refraction of light at the interface of the gel and liquid, but in practice, there may still exist a residual refractive index mismatch [13–16]. A previous study reported the resulting artifacts, mostly located around the edge of the sample, and proposed a computational method to correct the refractive index mismatch [6]. This reconstruction strategy required to calculate a shift matrix of each voxel to realign the images and remains computationally expensive.

In this work, we propose a simple ray optics model to remove artifacts induced by the RI mismatch between the cylindrical gel and the surrounding liquid. Our contributions are two-fold: we revisit this type of RI mismatch and its interpretation as a virtual cylindrical lens. We approximate the virtual lensing effect using a cone beam model. We discuss the validity of this model and point out the importance of considering the displacement of the rotating cylinder. Second, we use our model to correct the artifacts with a computationally efficient algorithm on experimental images of fluorescent beads.

In an OPT experiment, the sample is rotated to a series of angular positions to produce a set of 2D projections. Before the experiment, the rotation axis is carefully adjusted to be perpendicular to the optical axis so that the projection data of one slice of the volume is recorded in a row of pixels on the detector [2]. When there is no refraction, diffraction, scattering or defocusing, the emitted light propagates through the sample, the index-matching liquid and the telecentric lens system in parallel straight lines (see Fig. 1). Therefore, the standard forward model for OPT is the Radon transform [17, 18]. Consequently a 3D image of the sample can be restored in a slice by slice fashion using the Filtered Backprojection (FBP) algorithm [2, 17].

In reality, when there exists a refractive index mismatch be-

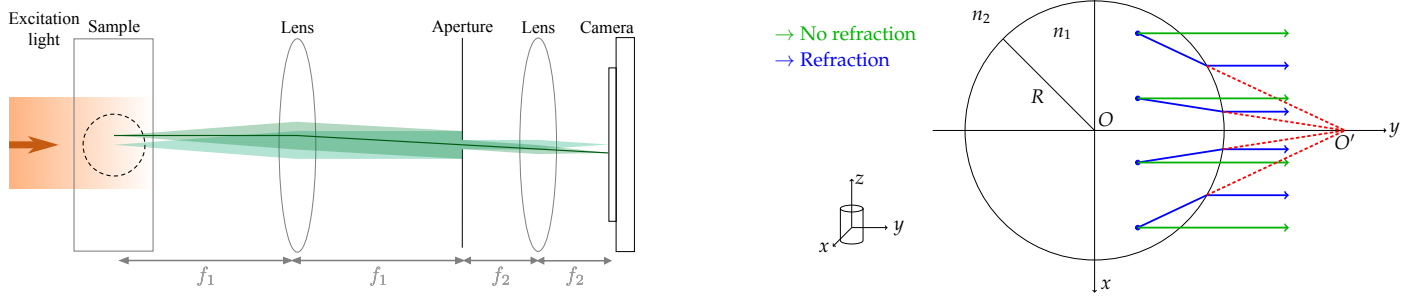


Fig. 1. Emission OPT geometry in the ideal case and with refractive index mismatch. (Left) Diagram of an emission OPT experiment viewed from the top. The sample, fixed in agarose gel, is placed inside a glass container filled with an embedding liquid. The fluorophores inside the sample emit light that propagates through the telecentric lens system and gets recorded by the camera. (Right) Comparison between of ray geometries between the ideal case (green) and with refractive index mismatch (blue). Only rays parallel to the optical axis are considered due to the low-NA fluorescence collection in OPT. The refractive index of the sample n_1 differs from the one of the embedding medium n_2 ($n_1 < n_2$ here), and this creates a lensing effect, with a virtual focus at position O' on the optical axis.

tween the sample and the embedding liquid, the path of the light propagation is altered so that the parallel beam assumption no longer holds. Consider a 2D transverse slice of the sample in the liquid bath as depicted in Fig. 1. We denote the refractive index of the agarose gel and the liquid bath as n_1 and n_2 , respectively, and the radius of the cylinder as R . Without refractive index mismatch, i.e. $n_1 = n_2$, the emitted light that will be recorded by the detector follows parallel straight lines as it travels through the sample, the liquid bath and finally the flat wall of the cuvette (see the green lines in Fig. 1). When $n_1 \neq n_2$, light will be refracted at the interface of the circle and the liquid bath. The refracted light propagation is illustrated by the blue lines in Fig. 1. When we extend the incident rays (blue lines inside the circle in Fig. 1), they intersect at a point O' on the y axis (see dotted red lines in Fig. 1). Hence, the front wall of the circle can be seen as a diverging lens whose virtual focus O' is on the optical axis. These incident rays inside this circle can then be approximated by a fan beam, the origin of which coincides with the virtual focus.

Such a picture is based on two simplifying assumptions which help us to keep our model computationally tractable. First, we make the paraxial assumption; namely that these point emitters are close to the optical axis. Second, we consider the difference in refractive index to be small enough ($|n_2 - n_1| \ll n_1$), so that the resulting origin of the fan beam is far away from the cylinder. Under these assumptions, the location y_0 of the origin of O' of the converging beam is proven to depend on the radius R of the cylinder and the refractive indices n_1, n_2 according to

$$y_0 = \frac{n_1}{n_2 - n_1} R. \quad (1)$$

A detailed derivation of Eq. (1) is provided in the appendix.

Thus, there is a mismatch between the actual physical model and the one typically used for reconstruction with a parallel beam geometry. Although the proposed virtual lens model is an approximation of the actual physical model, we will show it is capable of reproducing and eventually correcting for these artifacts. This 2D analysis corresponds to a fan-beam model; however, under suitable conditions, we can also extend it to a cone beam model on thin stack of slices in 3D. Cone-beam geometries are common in other tomographic applications, hence, we leverage efficient implementations and reconstruction algorithms.

An additional physical effect to be considered is the displacement of the cylinder as it rotates. This happens when the axis

of rotation is shifted compared to the axis of the cylinder. With no refractive index mismatch, this would not affect the propagation of light but here its role is non-negligible. This has been hinted in [4] as the seagull artifacts are more or less pronounced depending on the cylinder position. In the appendix, we show that our cone-beam geometry remains a good approximation in this case as well. In practice, this rotating cylinder effect moves the origin of the cone beam closer to the sample.

To validate our method in modeling the refractive index mismatch, we simulate the setup of a real emission OPT experiment for imaging fluorescent beads. We use the cone beam model to generate projections with an origin position y_0 defined by $\frac{y_0}{R} = 5$, and then apply the FBP algorithm which corresponds to the ideal parallel beam forward model for reconstruction. Our phantom consists of 13 beads each of unit intensity and of size 5×5 px (one pixel is $2.45 \mu\text{m}$) embedded in a slice of a cylinder with radius $R = 1024$ px contained in a square cuvette of length 2048 px. Additionally, it will be important to consider here that the depth of field in OPT usually covers only half of the sample, in contrast with X-ray tomography. To approximate the out-of-focus phenomenon of the other half, we implement rotation angles over both $[0, \pi)$ and $[0, 2\pi)$.

Fig. 2 (d) shows a vertical section of the original reconstruction of size 2048^2 px. The bead at the exact center of the image is free of artifacts. As the distance of the bead to the center of the image increases, the seagull artifacts become more pronounced, which is reflected in the size of their “wings”. To get a close-up view of the details, we choose one bead with strong seagull artifacts and zoom in 16 times; its reconstructions using the rotation angles in $[0, \pi)$ and $[0, 2\pi)$ are respectively shown in Fig. 2 (b) and (c). The magnified ground truth image is provided in Fig. 2 (a) as a reference.

All the simulations have been performed using the Tomosipo toolbox [19], a wrapper for the tomographic reconstruction library ASTRA [20]. We have resorted to a cone beam geometry as this modality is common in tomography [21] and has already been implemented efficiently in Tomosipo. It enables us to speed up computation on CPU and GPU, and to use the already-implemented FDK algorithm for cone beam reconstruction [22]. This is crucial in OPT because to realize high resolution imaging of mesoscopic samples, a time- and memory-efficient reconstruction algorithm is required to process the huge-sized measurement dataset (1200 projections of 2048×2048 px each). Accurate models such as [6] would encounter computational

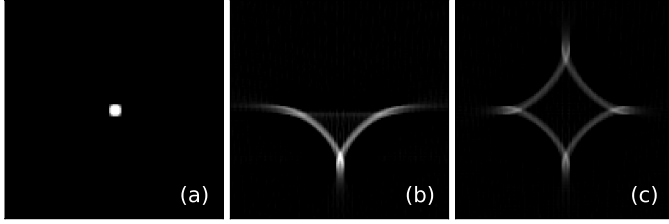


Fig. 2. A close-up view of the seagull artifacts in the reconstruction of a fluorescent bead due to refractive index mismatch with rotation angles on $[0, \pi)$ (b) and $[0, 2\pi)$ (c) compared to the ground truth (a).

bottlenecks and become infeasible for high temporal and spatial imaging.

Next, we show how to mitigate the “seagull” artifacts on experimental data of fluorescent beads. $1\ \mu\text{m}$ fluorescent FITC-labeled microspheres based on melamine resin (90305-5ML-F, Sigma) were used as specimen following the preparation procedure described in [4]. Approximately 0.01 ml of particle solution were mixed to 10 ml of 1.5% agarose before molding to achieve a nearly-colloidal solution. The acquisition was performed shortly after preparation to avoid undesired fluorescence quenching of the signal. The refractive index mismatch between agarose and BABB immersion liquid is roughly estimated around 0.1.

Before the reconstruction, two preliminary preprocessing steps were required. First, we remove possible artifacts due to other model mismatch, in particular, the misaligned rotation center that is a common issue [18, 23, 24] for OPT images. Because the fluorescent beads sample is very sparse compared to an actual biological sample, the reconstruction of beads carries too little information for the commonly-adopted method based on the maximum variance of a reconstructed slice [4, 11, 23]. We instead perform a grid search and determine the best estimate of the center of rotation when the “circle”-shaped artifacts caused by wrong rotation center vanish. Second, the origin guess provided in Eq. (1) does not yield good reconstruction results due to the rotating cylinder effect mentioned before and the fact that the refractive index of the agarose gel may change over time. To be precise, the RI of the agarose gel tends to match the one of the surrounding liquid (e.g. BABB) by molecular diffusion. This process may extend over the standard clearing protocol time and result in permanent residual mismatch. We thus propose a method to automatically determine the origin of the cone beam by minimizing a loss metric. Specifically, our loss metric is

$$E_{\text{loss}} = 1 - \frac{\sum_{i \in \Omega_{\text{in}}} I_i}{\sum_{i \in \Omega_{\text{total}}} I_i}, \quad (2)$$

where Ω_{total} is a square region that fully encloses the whole “seagull”, Ω_{in} is a smaller square region enclosing only the central part of a bead (see Fig. 3 (b), (d) and (f)), and I_i denotes the intensity at pixel i . E_{loss} hence indicates how concentrated the intensity distribution is around the center of a bead. The smaller E_{loss} is, the less energy is spread outside the true location of the bead, and the better the reconstruction is. Fig. 3 shows the energy loss curves of five different beads at varied locations in the FOV. We observe that the energy loss curves for all five beads behave similarly and achieve their minima around almost the same value. This means that the optimal origin guesses for three different beads are stable, proving the robustness of the proposed automatic calibration. We thus adopt the average value

$\mu = \frac{y_0}{R} = 4.4$ as the optimal cone origin for all the beads in the reconstruction. The mismatch with the value of 14.5 from Eq. (1) highlights the importance to have this automatic calibration to take into account the additional effect of the rotating cylinder.

In Fig. 3, we show the reconstructions results using a parallel-beam model or our approach. We can observe the clear radial dependence of the size of the seagull artifacts. Our proposed cone beam model successfully mitigated the artifacts, especially for the highlighted beads in the red boxes. To quantify the improvement of our method, we provide the intensity profiles along the direction of maximal variance of the uncorrected and corrected reconstructions of the this bead in Fig. 3 (f). The Full Width Half Maximum (FWHM) along the direction of maximum variance, calculated based on the Gaussian fit, is $47\ \mu\text{m}$ and $22\ \mu\text{m}$ for Fig. 3 (d) and (e), respectively. This means that we obtain a 52% increase in resolution thanks to the correction of artifacts.

To conclude, this work presents a model of the refractive index mismatch in emission OPT as a virtual lens. Using this cone beam model, we can reproduce the “seagull” artifacts observed in real emission OPT experiments by simulating the model mismatch in numerical experiments. To achieve best performance in practice, we propose a fast approach that automatically determines the optimal cone origin needed for reconstruction and validate our methods on experimental data of fluorescent beads. Our results show that the cone beam model with an optimized origin successfully mitigates the seagull-shaped artifacts and increased the resolution of the reconstruction in both x and y directions.

Future research directions include a more precise modeling of both the finite depth-of-field and the rotating cylinder. This work based on emission OPT only has to consider the RI mismatch on one side of the sample along the light path. It can be extended to transmission OPT by taking into account the RI mismatch on both sides of the sample. Finally, cone beam reconstructions could also be used with continuous samples, to improve the image contrast which is degraded by these artifacts. The automatic calibration scheme could in this case be extended based on an image quality metric.

FUNDING

Y.L., J.D., and M.U. acknowledge funding from European Research Council (ERC) under the European Union’s Horizon 2020 research and innovation programme (Grant Agreement No. 692726 GlobalBioIm).

ACKNOWLEDGMENTS

We would like to thank Thanh-an Pham for useful discussions and Eric Sinner for his help in making the figures.

DISCLOSURES

The authors declare no conflicts of interest. See [appendix](#) for supporting content.

REFERENCES

1. J. Sharpe, U. Ahlgren, P. Perry, B. Hill, A. Ross, J. Hecksher-Sørensen, R. Baldock, and D. Davidson, *Sci. (New York, N.Y.)* **296**, 541 (2002).
2. J. Sharpe, *Annu. review biomedical engineering* **6**, 209 (2004).
3. A. Darrell, H. Meyer, U. Birk, K. Marias, M. Brady, and J. Ripoll, “Maximum likelihood reconstruction for fluorescence optical projection tomography,” in *2008 8th IEEE International Conference on Bioinformatics and BioEngineering*, (2008), pp. 1–6.

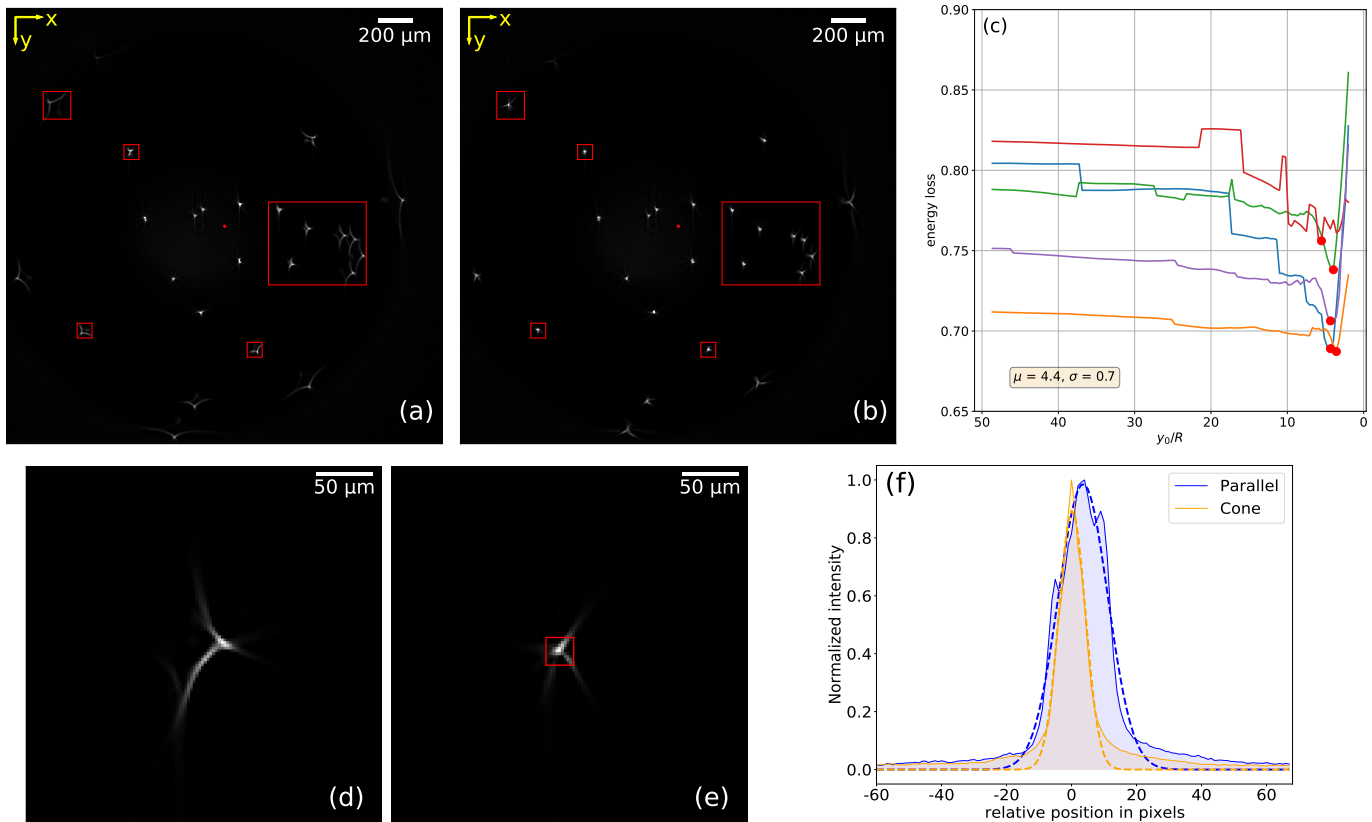


Fig. 3. (a) and (b): Comparison of the reconstructions of the 3D volume integrated along z axis using parallel beam model (a) and cone beam model (b). with seagull artifact of fluorescent beads. (c): Energy loss curves of 5 different beads over a range of origin guess. The red point on each curve indicates the minimum. (d) and (e): Comparison of the same slice of the 3D reconstructions of a bead zoomed in 16 times using parallel (d) and cone (e) beam model. The red square in (e) is the region Ω_{in} used to compute the energy loss. (f): Intensity profiles along the direction of maximum variance of bead in (d) and (e). The blue and orange lines represent the intensity profiles for parallel and cone beam model respectively. The dashed blue and orange lines represent the fitted Gaussian PSFs for the intensity profiles.

- C. Schmidt, A. L. Planchette, D. Nguyen, G. Giardina, Y. Neuenschwander, M. D. Franco, A. Mylonas, A. C. Descloux, E. Pomarico, A. Radenovic, and J. Extermann, *Biomed. Opt. Express* **12**, 3619 (2021).
- D. Nguyen, P. J. Marchand, A. L. Planchette, J. Nilsson, M. Sison, J. Extermann, A. Lopez, M. Sylwestrzak, J. Sordet-Dessimoz, A. Schmidt-Christensen, D. Holmberg, D. V. D. Ville, and T. Lasser, *Biomed. Opt. Express* **8**, 5637 (2017).
- U. J. Birk, A. Darrell, N. Konstantinides, A. Sarasa-Renedo, and J. Ripoll, *Appl. Opt.* **50**, 392 (2011).
- A. C. Kak and M. Slaney, *Principles of Computerized Tomographic Imaging* (Society for Industrial and Applied Mathematics, 2001).
- B. W. Lindsey and J. Kaslin, *Zebrafish* **14**, 574 (2017). PMID: 28296621.
- J. R. Walls, J. G. Sled, J. Sharpe, and R. M. Henkelman, *Phys. Medicine Biol.* **50**, 4645 (2005).
- J. Michalek, *Microsc. Microanal.* **21**, 1602–1615 (2015).
- V. C. Torres, C. Li, W. Zhou, J. G. Brankov, and K. M. Tichauer, *Appl. Opt.* **60**, 135 (2021).
- G. C. Antonopoulos, D. Pscheniza, R.-A. Lorbeer, M. Heidrich, K. Schwanke, R. Zweigerdt, T. Ripken, and H. Meyer, "Correction of image artifacts caused by refractive index gradients in scanning laser optical tomography," in *Three-Dimensional and Multidimensional Microscopy: Image Acquisition and Processing XXI*, vol. 8949 T. G. Brown, C. J. Cogswell, and T. Wilson, eds., International Society for Optics and Photonics (SPIE, 2014), pp. 21 – 26.
- S. Doran, K. Koerkamp, M. Bero, P. Jenneson, E. Morton, and W. Gilboy, *Phys. medicine biology* **46**, 3191 (2002).
- K. Islam, J. Dempsey, M. Ranade, M. Maryanski, and D. Low, *Med. physics* **30**, 2159 (2003).
- M. Haidekker, *Comput. methods programs biomedicine* **80**, 225 (2006).
- A. Marcos-Vidal and J. Ripoll, *Opt. Lasers Eng.* **135**, 106191 (2020).
- F. Natterer, *The Mathematics of Computerized Tomography* (Society for Industrial and Applied Mathematics, USA, 2001).
- V. Koljonen, O. Koskela, T. Montonen, A. Rezaei, B. Belay, E. Figueiras, J. Hyttinen, and S. Pursiainen, *Phys. Medicine Biol.* **64** (2019).
- A. Hendriksen, D. Schut, W. J. Palenstijn, N. Viganò, J. Kim, D. Pelt, T. van Leeuwen, and j. batenburg, *Opt. Express* (2021).
- W. van Aarle, W. J. Palenstijn, J. Cant, E. Janssens, F. Bleichrodt, A. Dabrovolski, J. D. Beenhouwer, K. J. Batenburg, and J. Sijbers, *Opt. Express* **24**, 25129 (2016).
- M. Grass, T. Köhler, and R. Proksa, *Phys. Medicine Biol.* **45**, 329 (1999).
- L. A. Feldkamp, L. C. Davis, and J. W. Kress, *J. Opt. Soc. Am. A* **1**, 612 (1984).
- J. R. Walls, J. G. Sled, J. Sharpe, and R. M. Henkelman, *Phys. Medicine Biol.* **52**, 2775 (2007).
- O. Koskela, T. Montonen, B. Belay, E. Figueiras, S. Pursiainen, and J. Hyttinen, *Sci. Reports* **9** (2019).

FULL REFERENCES

1. J. Sharpe, U. Ahlgren, P. Perry, B. Hill, A. Ross, J. Hecksher-Sørensen, R. Baldock, and D. Davidson, "Optical projection tomography as a tool for 3d microscopy and gene expression studies," *Sci. (New York, N.Y.)* **296**, 541–5 (2002).
2. J. Sharpe, "Optical projection tomography," *Annu. review biomedical engineering* **6**, 209–28 (2004).
3. A. Darrell, H. Meyer, U. Birk, K. Marias, M. Brady, and J. Ripoll, "Maximum likelihood reconstruction for fluorescence optical projection tomography," in *2008 8th IEEE International Conference on BioInformatics and BioEngineering*, (2008), pp. 1–6.
4. C. Schmidt, A. L. Planchette, D. Nguyen, G. Giardina, Y. Neuenschwander, M. D. Franco, A. Mylonas, A. C. Descloux, E. Pomarico, A. Radenovic, and J. Extermann, "High resolution optical projection tomography platform for multispectral imaging of the mouse gut," *Biomed. Opt. Express* **12**, 3619–3629 (2021).
5. D. Nguyen, P. J. Marchand, A. L. Planchette, J. Nilsson, M. Sison, J. Extermann, A. Lopez, M. Sylwestrzak, J. Sordet-Dessimoz, A. Schmidt-Christensen, D. Holmberg, D. V. D. Ville, and T. Lasser, "Optical projection tomography for rapid whole mouse brain imaging," *Biomed. Opt. Express* **8**, 5637–5650 (2017).
6. U. J. Birk, A. Darrell, N. Konstantinides, A. Sarasa-Renedo, and J. Ripoll, "Improved reconstructions and generalized filtered back projection for optical projection tomography," *Appl. Opt.* **50**, 392–398 (2011).
7. A. C. Kak and M. Slaney, *Principles of Computerized Tomographic Imaging* (Society for Industrial and Applied Mathematics, 2001).
8. B. W. Lindsey and J. Kaslin, "Optical projection tomography as a novel method to visualize and quantitate whole-brain patterns of cell proliferation in the adult zebrafish brain," *Zebrafish* **14**, 574–577 (2017). PMID: 28296621.
9. J. R. Walls, J. G. Sled, J. Sharpe, and R. M. Henkelman, "Correction of artefacts in optical projection tomography," *Phys. Medicine Biol.* **50**, 4645–4665 (2005).
10. J. Michalek, "Total variation-based reduction of streak artifacts, ring artifacts and noise in 3d reconstruction from optical projection tomography," *Microsc. Microanal.* **21**, 1602–1615 (2015).
11. V. C. Torres, C. Li, W. Zhou, J. G. Brankov, and K. M. Tichauer, "Characterization of an angular domain fluorescence optical projection tomography system for mesoscopic lymph node imaging," *Appl. Opt.* **60**, 135–146 (2021).
12. G. C. Antonopoulos, D. Pscheniza, R.-A. Lorbeer, M. Heidrich, K. Schwanke, R. Zweigert, T. Ripken, and H. Meyer, "Correction of image artifacts caused by refractive index gradients in scanning laser optical tomography," in *Three-Dimensional and Multidimensional Microscopy: Image Acquisition and Processing XXI*, vol. 8949 T. G. Brown, C. J. Cogswell, and T. Wilson, eds., International Society for Optics and Photonics (SPIE, 2014), pp. 21 – 26.
13. S. Doran, K. Koerkamp, M. Bero, P. Jenneson, E. Morton, and W. Gilboy, "A ccd-based optical ct scanner for high-resolution 3d imaging of radiation dose distributions: Equipment specifications, optical simulations and preliminary results," *Phys. medicine biology* **46**, 3191–213 (2002).
14. K. Islam, J. Dempsey, M. Ranade, M. Maryanski, and D. Low, "Initial evaluation of commercial optical ct-based 3d gel dosimeter," *Med. physics* **30**, 2159–68 (2003).
15. M. Haidekker, "Optical transillumination tomography with tolerance against refraction mismatch," *Comput. methods programs biomedicine* **80**, 225–35 (2006).
16. A. Marcos-Vidal and J. Ripoll, "Recent advances in optical tomography in low scattering media," *Opt. Lasers Eng.* **135**, 106191 (2020).
17. F. Natterer, *The Mathematics of Computerized Tomography* (Society for Industrial and Applied Mathematics, USA, 2001).
18. V. Koljonen, O. Koskela, T. Montonen, A. Rezaei, B. Belay, E. Figueiras, J. Hyttinen, and S. Pursiainen, "A mathematical model and iterative inversion for fluorescent optical projection tomography," *Phys. Medicine Biol.* **64** (2019).
19. A. Hendriksen, D. Schut, W. J. Palenstijn, N. Viganò, J. Kim, D. Pelt, T. van Leeuwen, and j. batenburg, "Tomosipo: Fast, flexible, and convenient 3D tomography for complex scanning geometries in Python," *Opt. Express* (2021).
20. W. van Aarle, W. J. Palenstijn, J. Cant, E. Janssens, F. Bleichrodt, A. Dabrovolski, J. D. Beenhouwer, K. J. Batenburg, and J. Sijbers, "Fast and flexible x-ray tomography using the astra toolbox," *Opt. Express* **24**, 25129–25147 (2016).
21. M. Grass, T. Köhler, and R. Proksa, "3d cone-beam CT reconstruction for circular trajectories," *Phys. Medicine Biol.* **45**, 329–347 (1999).
22. L. A. Feldkamp, L. C. Davis, and J. W. Kress, "Practical cone-beam algorithm," *J. Opt. Soc. Am. A* **1**, 612–619 (1984).
23. J. R. Walls, J. G. Sled, J. Sharpe, and R. M. Henkelman, "Resolution improvement in emission optical projection tomography," *Phys. Medicine Biol.* **52**, 2775–2790 (2007).
24. O. Koskela, T. Montonen, B. Belay, E. Figueiras, S. Pursiainen, and J. Hyttinen, "Gaussian light model in brightfield optical projection tomography," *Sci. Reports* **9** (2019).

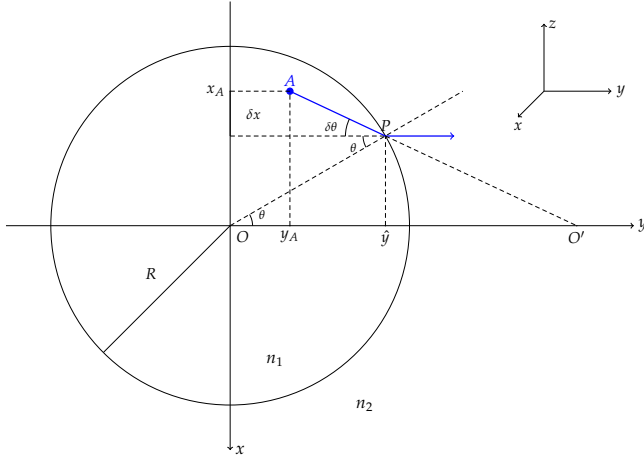


Fig. 4. Geometry of light refraction at the interface of the cylinder and the embedding medium. The refractive indices inside and outside the circle are n_1 and n_2 , respectively.

A. DERIVATION OF THE CONE BEAM EQUIVALENCE

To calculate the location of the virtual focus of the diverging lens, i.e. the origin of the cone beam, we focus on a 2D transverse slice of the cylinder, i.e. a disk (See Fig. 4).

The main quantities that will be useful are the following:

- R the radius of the disk
- $A(x_A, y_A)$ the emitter position
- $P(\hat{x}, \hat{y})$ the incident point on the cylinder surface
- δx the vertical displacement between the emitter and P
- O' the intersection of the incident ray with the y -axis
- θ the refracted angle such that the refracted ray is parallel to the optical axis
- $\theta + \delta\theta$ the incident angle
- $\Delta n = n_2 - n_1$ that we assume to be small

Snell's law gives

$$n_2 \sin \theta = n_1 \sin(\theta + \delta\theta) \approx n_1(\sin \theta + \delta\theta \cos \theta), \quad (3)$$

where we performed a first order Taylor expansion. Eq. (3) gives

$$\delta\theta = \frac{n_2 - n_1}{n_1} \tan \theta. \quad (4)$$

Because $\delta\theta \ll 1$, in the right triangle with longest side AP ,

$$\delta\theta \approx \tan \delta\theta = \frac{\delta x}{\hat{y} - y_A}. \quad (5)$$

with $\hat{y} = \sqrt{R^2 - (x_A - \delta x)^2} = \sqrt{R^2 - x_A^2} + \mathcal{O}(\Delta n)$. Combining Eq. (5) and Eq. (4) we obtain

$$\delta x = (\hat{y} - y_A) \frac{\Delta n}{n_1} \tan \theta. \quad (6)$$

On the other hand, we also have:

$$\tan \theta = \frac{x_A - \delta x}{\hat{y}}. \quad (7)$$

Substituting Eq. (7) into Eq. (6) yields at order 1 in Δn :

$$\delta x = (\hat{y} - y_A) \frac{\Delta n x_A}{n_1 \hat{y}}. \quad (8)$$

The equation of the line (AP) is thus:

$$y - y_A = \frac{\hat{y} - y_A}{\delta x} (x - x_A) \quad (9)$$

$$= \frac{n_1 \hat{y}}{\Delta n x_A} (x - x_A). \quad (10)$$

The intersection for which $x = 0$ corresponds to:

$$y_0 = y_A - \frac{n_1 \sqrt{R^2 - x_A^2}}{\Delta n}. \quad (11)$$

For $\Delta n \ll 1$, the first term is negligible compared to the second one and for $x_A \ll R$ (i.e. for points close to the optical axis, which corresponds to the paraxial approximation), we obtain:

$$y_0 = \frac{n_1 R}{\Delta n}. \quad (12)$$

The coordinates of this intersection point O' do not depend on the position of our point A in the paraxial approximation. We thus obtain a fan beam geometry where all the rays inside the cylinder intersect at O' . When $n_1 = n_2$, the origin of the cone beam becomes $+\infty$, hence the cone reduces to the standard parallel beam model as expected.

B. CONE BEAM ORIGIN SHIFT DUE TO OFF-CENTER ROTATION

While we have shown that the index mismatch transforms the parallel problem into a conic one, the center that yields the optimal FDK reconstruction is not exactly the y_0 predicted by Eq. (12), but rather a y_r that is significantly closer to the object ($y_0 - y_r > 0$). Following recent evidence regarding the effects of recalibration on seagull artifacts [4], we have established experimentally that a miscentering of the cylinder with respect to the axis of the turning platform is at the origin of this offset.

To reconcile the conic geometry motivated in 12 with this newly-characterized experimental error, we proceed to show that the offset rotation accumulates the original projections in a way that generates an alternative cone with its center displaced towards the origin. Indeed, even when misaligned, the platform still rotates the sample fully and hence generates complete tomographic data. The center of a cone beam corresponds to the position through which a maximum of light rays pass; we thus look for the point where the intensity flux is at its maximum.

Since the effect of the rotation on the y direction is negligible because $y_0 \gg R$, we focus instead on the movement induced in the x direction. This displacement can be expressed as $r \cos \theta$, where θ is the angle of rotation and r the distance between the center of the sample and the true axis. At each angle of rotation, the rays originate a light cone that is viewed from y_0 with an angle ψ , which in turn depends on R (Fig. 5). These cones accumulate on the line segment $[-r, r] \times \{y_0\}$ (blue in Fig. 5) according to the amplitude of rotation.

Let us therefore change to a coordinate system (x, y') centered on $(0, y_0)$ and with the axis of symmetry flipped, i.e. $y = y_0 - y'$. Using this reference, the finite domain limits the spatial influence of the rays, making them all coincide at $x = 0, y' = y'^* := r \cot(\psi/2)$ and thus creating an equivalent cone center under

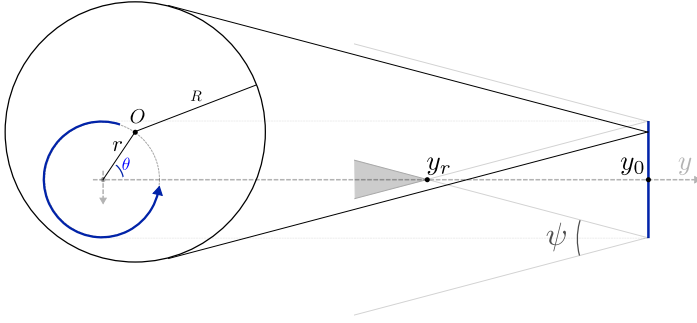


Fig. 5. Effect of the off-centered rotation of the sample on the center of the cone beam. The bigger black disk corresponds to the cylinder in Fig. 4, whereas the greyish inner circle represents its orbit around the true center (size exaggerated). The rotation trajectory (in blue) is translated into an oscillation (also in blue) of the cone's center that generates an alternative cone closer to the sample.

fairly general conditions. To show this, we use $f(x, y')$ to model the brightness within the span of each cone and $w(x)$ to weight their contributions in a way that reflects how the projections concentrate at the poles. Together, they multiply to yield a weighted intensity flux

$$g(x, y') = f\left(\sqrt{x^2 + y'^2}\right) w(x). \quad (13)$$

All contributions can then be combined by integrating over the x movement as

$$I(y')/2 = \begin{cases} \int_0^r g(x, y') dx & y' \geq y'^*, \\ \int_0^{y' \tan(\psi/2)} g(x, y') dx & y' < y'^*, \end{cases} \quad (14)$$

which is split into two components precisely because the offset rotation has finite amplitude. Note that the weighted intensity energy I is continuous as y'^* is the solution to $r = y' \tan(\psi/2)$, and that the factor of 2 appears thanks to the symmetry of g with respect to the integration domain.

The maximum of I is attained at y'^* when g is constant, thus originating a (uniform) cone beam closer ($y'^* > 0$) to the object. We now show that such a maximum still exists under quite general physical conditions. Since brightness is to be conserved, one expects the divergence of f to vanish in the radial direction ρ of the corresponding polar reference system, yielding $\nabla \cdot f = \rho^{-1} \partial(\rho f) / \partial \rho = 0$ and thus $f \propto \rho^{-1} = 1/\sqrt{x^2 + y'^2}$. On the other hand, the weighting function can be thought proportional to the derivative of the geometric projection of the rotation, i.e. $w \propto |\sin(\pi x/2r)|$. Together, f and w combine into a $g \propto \sin(\pi x/2r) / \sqrt{x^2 + y'^2}$ that makes I monotonically increasing for $y' < y'^*$ and decreasing for $y' > y'^*$ because the integration domain shrinks progressively. And therefore with a maximum at $y'^* = \arg\max_{y' \in [0, \infty)} I$, showcasing the formation of an equivalent cone beam that is closer to the object. With respect to the original reference system, the shifted cone beam center is at $y_r = y_0 - y'^*$.

To find the center y_r of the cone beam in practice, we resort to the automatic calibration scheme presented in the main text because it is more robust against seagull artifacts: it finds a center that is consistent across several beads without the need to estimate additional experimental parameters such as r , y_0 , or ψ .